



Cite this: DOI: 10.1039/d1dt00057h

# Ba<sub>2</sub>Ln<sub>1-x</sub>Mn<sub>2</sub>Te<sub>5</sub> (Ln = Pr, Gd, and Yb; x = Ln vacancy): syntheses, crystal structures, optical, resistivity, and electronic structure†

Gopabandhu Panigrahi,<sup>a</sup> Subhendu Jana,<sup>a</sup> Mohd Ishtiyak,<sup>a</sup> S. Narayanswamy,<sup>b</sup> Pinaki P. Bhattacharjee,<sup>b</sup> K. V. Ramanujachary,<sup>c</sup> Manish K. Niranjan<sup>d</sup> and Jai Prakash<sup>\*a</sup>

Three new isostructural quaternary tellurides, Ba<sub>2</sub>Ln<sub>1-x</sub>Mn<sub>2</sub>Te<sub>5</sub> (Ln = Pr, Gd, and Yb), have been synthesized by the molten-flux method at 1273 K. The single-crystal X-ray diffraction studies at 298(2) K showed that Ba<sub>2</sub>Ln<sub>1-x</sub>Mn<sub>2</sub>Te<sub>5</sub> crystallize in the space group C<sub>2h</sub><sup>3</sup> –C2/m of the monoclinic crystal system. There are six unique crystallographic sites in this structure's asymmetric unit: one Ba site, one Ln site, one Mn site, and three Te sites. The Ln site in the Ba<sub>2</sub>Ln<sub>1-x</sub>Mn<sub>2</sub>Te<sub>5</sub> structure is partially filled, which leaves about one-third of the Ln sites vacant (□) for Pr and Gd compounds. These structures do not contain any homoatomic or metallic bonding and can be charge-balanced as (Ba<sup>2+</sup>)<sub>2</sub>(Gd/Pr<sup>3+</sup>)<sub>2/3</sub>(Mn<sup>2+</sup>)<sub>2</sub>(Te<sup>2-</sup>)<sub>5</sub>. The refined composition for the Yb compound is Ba<sub>2</sub>Yb<sub>0.74(1)</sub>Mn<sub>2</sub>Te<sub>5</sub> and can be charge-balanced with a mixed valence state of Yb<sup>2+</sup>/Yb<sup>3+</sup>. The crystal structures of Ba<sub>2</sub>Ln<sub>1-x</sub>Mn<sub>2</sub>Te<sub>5</sub> consist of complex layers of  $\frac{2}{\infty}$ [Ln<sub>1-x</sub>Mn<sub>2</sub>Te<sub>5</sub>]<sup>4-</sup> stacked along the [100] direction, with Ba<sup>2+</sup> cations separating these layers. The Ln atoms are bound to six Te atoms that form a distorted octahedral geometry around the central Ln atom. Each Mn atom in this structure is coordinated to four Te atoms in a distorted tetrahedral fashion. These LnTe<sub>6</sub> and MnTe<sub>4</sub> units are the main building blocks of the Ba<sub>2</sub>Ln<sub>1-x</sub>Mn<sub>2</sub>Te<sub>5</sub> structure. The optical absorption study performed on a polycrystalline Ba<sub>2</sub>Gd<sub>2/3</sub>Mn<sub>2</sub>Te<sub>5</sub> sample reveals a direct bandgap of 1.06(2) eV consistent with the DFT study. A semiconducting behavior was also observed for polycrystalline Ba<sub>2</sub>Gd<sub>2/3</sub>Mn<sub>2</sub>Te<sub>5</sub> from the resistivity study. The temperature-dependent magnetic studies on a polycrystalline sample of Ba<sub>2</sub>Gd<sub>2/3</sub>Mn<sub>2</sub>Te<sub>5</sub> did not reveal any long-range magnetic order down to 5 K. The effective magnetic moment (μ<sub>eff</sub>) of 10.37μ<sub>B</sub> calculated using the Curie–Weiss law is in good agreement with the theoretical value (μ<sub>cal</sub>) of 10.58μ<sub>B</sub>.

Received 7th January 2021.

Accepted 7th April 2021

DOI: 10.1039/d1dt00057h

rsc.li/dalton

## 1. Introduction

Transition-metal (M) based chalcogenides containing alkali (A) or alkaline earth (AE) metals have long been a subject of interest due to their applications in various fields, such as thermoelectric materials,<sup>1,2</sup> transparent conductivity,<sup>3</sup> cataly-

sis,<sup>4</sup> magnetism,<sup>5,6</sup> and superconductivity.<sup>7</sup> Similarly, the ternary chalcogenides of lanthanides (Ln) with alkali or alkaline earth metals are also well-known for their rich crystal-chemistry and a variety of physical properties.<sup>8</sup> The main framework of most of these chalcogenide crystal structures is formed by the sharing of transition metal and chalcogen-based octahedra and/or tetrahedra.<sup>9</sup> The addition of lanthanides that prefer octahedral<sup>10</sup> and trigonal prism-like geometries<sup>11</sup> to transition-metal based chalcogenides results in the stabilization of various new complex low-dimensional materials that display a variety of one-dimensional, layered, and tunnel structures.<sup>12,13</sup> Among these, layered chalcogenides have additional advantages due to the possibility of fine-tuning their physical properties using host-guest intercalation as well as controlling their electronic properties by manipulating the chemical composition of the spacing layer.<sup>14</sup> For example, the superconducting transition temperature (T<sub>c</sub>) of Fe-based chalcogenides could be enhanced from 8 K to 30–46 K with various intercalated guest species.<sup>15,16</sup>

<sup>a</sup>Department of Chemistry, Indian Institute of Technology Hyderabad, Kandi, Sangareddy, Telangana 502285, India. E-mail: jaiprakash@chy.iith.ac.in

<sup>b</sup>Department of Materials Science & Metallurgical Engineering, Indian Institute of Technology Hyderabad, Kandi, Sangareddy, Telangana 502285, India

<sup>c</sup>Department of Chemistry and Biochemistry, Rowan University, Glassboro, New Jersey 08028, USA

<sup>d</sup>Department of Physics, Indian Institute of Technology Hyderabad, Kandi, Sangareddy, Telangana 502285, India

†Electronic supplementary information (ESI) available: Experimental details, PXRD patterns, and details of the crystallographic parameters for Ba<sub>2</sub>Ln<sub>2/3</sub>□<sub>1/3</sub>Mn<sub>2</sub>Te<sub>5</sub> (Ln = Pr, Gd, and Yb). CCDC 2049695, 1961083, and 2049699 for Pr, Gd, and Yb-based structures, respectively. For ESI and crystallographic data in CIF or other electronic format see DOI: 10.1039/d1dt00057h

Furthermore, the quaternary compounds of transition and lanthanide metal-based chalcogenides are expected to show complex magnetic behavior due to the possible exchange–correlation between the d-electrons of M atoms and 4f-electrons of Ln atoms.<sup>17</sup> Therefore, the crystal-chemistry and the associated physical properties of the quaternary chalcogenide compounds that contain both transition metals and lanthanides are indeed very intriguing. For example, compounds like  $\text{BaLn}_2\text{ZnS}_5$  (Ln = Ce, Pr, and Nd),<sup>18</sup>  $\text{BaNd}_2\text{MnS}_5$ ,<sup>18</sup>  $\text{BaLn}_2\text{MnS}_5$  (Ln = La, Ce, and Pr),<sup>19</sup>  $\text{BaGdCuSe}_3$ ,<sup>20</sup>  $\text{BaGdCuS}_3$ ,<sup>20</sup> and  $\text{BaNdAgTe}_3$ <sup>10</sup> show interesting magnetic properties. Examples of quaternary chalcogenides that show optical properties are  $\text{CsLnCdTe}_3$  (Ln = La, Pr, Nd, Sm, Gd, Tm, and Lu),<sup>21</sup>  $\text{CsLnMnSe}_3$  (Ln = Sm, Gd, Tb, Dy, Ho, Er, Tm, Yb, and Y),<sup>22</sup>  $\text{BaLaCuS}_3$ ,<sup>20</sup> and  $\text{BaLaCuSe}_3$ .<sup>20</sup> Recent theoretical studies on these 1113-type compounds show that these compounds have the potential to exhibit excellent thermoelectric properties.<sup>23</sup>

The phase-diagrams of ternary metal chalcogenides are relatively well studied as compared to quaternary metal chalcogenides. As a result, the number of phases known in the quaternary AE–Ln–M–Q system are fewer than those known in the corresponding ternary AE/Ln/Q or AE/M/Q systems. So far, a total of about fifty-three compounds are known in the AE–Ln–M–Q quaternary system.<sup>24</sup> These compounds can be broadly divided into four families based on their compositions:  $\text{AELnMQ}_3$  (1-1-1-3 type),  $\text{Ba}_4\text{Ln}_2\text{CdQ}_{10}$  (4-2-1-10 type),  $\text{BaLn}_2\text{MS}_5$  (1-2-1-5 type), and  $\text{Ba}_2\text{LaAg}_5\text{S}_6$  (2-1-5-6 type). The compounds with the general formula  $\text{Ba}_4\text{Ln}_2\text{CdQ}_{10}$ ,  $\text{BaLn}_2\text{MS}_5$ , and  $\text{Ba}_2\text{LaAg}_5\text{S}_6$  crystallize in the orthorhombic (space group:  $Cmc2_1$ ), tetragonal ( $I4/mcm$ ), and monoclinic ( $C2/m$ ) structures, respectively. The members of the 1-1-1-3 family adopt seven structure types depending on the nature and identity of metals and chalcogens.<sup>25</sup>

The crystal-chemistry of quaternary AE–Ln–M–Te tellurides is least explored, with only the 1-1-1-3 type of compounds known for the tellurides. Thus, we have initiated a study to explore the AE–Ln–M–Te quaternary system to discover new phases in an effort to study their structure–property relationships. In this article, we present the syntheses and crystal structures of three new members of this family,  $\text{Ba}_2\text{Ln}_{1-x}\text{Mn}_2\text{Te}_5$  (Ln = Pr, Gd, and Yb;  $x = \text{Ln vacancy}$ ), that show partial occupancy at the lanthanide sites. These layered quaternary tellurides are the first examples of compounds in the AE–Ln–M–Te system, which do not adopt the 1-1-1-3 type structure. The physical properties, including variable temperature resistivity and magnetization, of the  $\text{Ba}_2\text{Gd}_{2/3}\text{Mn}_2\text{Te}_5$  compound have also been studied in detail. We also present the electronic structure of this compound using density functional (DFT) calculations.

## 2. Experimental section

### 2.1. Syntheses

The following reactants were used as received for the syntheses of  $\text{Ba}_2\text{Ln}_{1-x}\text{Mn}_2\text{Te}_5$ : barium rod (Alfa Aesar 99+%), praseody-

mium (Alfa Aesar 99.9%), gadolinium (Alfa Aesar 99.9%), ytterbium lumps (Alfa Aesar 99.9%), manganese pieces (Alfa Aesar 99.9%), sodium chloride powder (Alfa Aesar 99.9%), and tellurium ingot (Sigma-Aldrich 99.999%). Prior to use, these chemicals were stored inside an argon-filled dry glove box due to their air and moisture sensitivity. All chemical manipulations were performed inside the argon-filled glove box. The surfaces of praseodymium, gadolinium, and ytterbium lumps were first shaved to remove the oxidized layer, and then small pieces of these metals were cut for the reactions.

**2.1.1. Syntheses of single crystals of  $\text{Ba}_2\text{Ln}_{1-x}\text{Mn}_2\text{Te}_5$  (Ln = Pr, Gd, and Yb).** Black crystals of the new quaternary phases,  $\text{Ba}_2\text{Ln}_{1-x}\text{Mn}_2\text{Te}_5$ , were first discovered by exploratory solid-state syntheses carried out in the Ba–Ln–Mn–Te system. The following synthesis methodology was used: the reactants were weighed and then transferred into a carbon-coated fused silica tube inside an Ar-filled dry glove box. These fused silica tubes were then sealed under vacuum (*ca.*  $10^{-4}$  Torr) with a flame torch. The heat treatment of the tubes containing the reaction mixture was carried out in a programmable muffle furnace. Many different heating profiles were explored to synthesize  $\text{Ba}_2\text{Ln}_{1-x}\text{Mn}_2\text{Te}_5$  crystals in good yield. The optimized best heating profile is as follows: the temperature of the furnace was increased from room temperature to 1273 K in 48 h, where the reaction mixtures dwelled for 48 h and then slowly cooled down to 1123 K at a cooling rate of 3 K  $\text{h}^{-1}$  followed by annealing for 48 h at 1123 K. Subsequently, the furnace temperature was cooled to 773 K at a rate of 4 K  $\text{h}^{-1}$ . Finally, the furnace was switched off and radiatively cooled to room temperature. The reaction tubes loaded with La and Ce were found broken after the heat-treatment.

**Synthesis of  $\text{Ba}_2\text{Pr}_{1-x}\text{Mn}_2\text{Te}_5$ .** Black irregular shaped crystals of  $\text{Ba}_2\text{Pr}_{1-x}\text{Mn}_2\text{Te}_5$  (Ba : Pr : Mn : Te in 6 : 2 : 6 : 15 ratio) were obtained from the reaction mixtures of Ba (24.6 mg, 0.179 mmol), Pr (8.4 mg, 0.060 mmol), Mn (9.8 mg, 0.179 mmol), Te (57.1 mg, 0.448 mmol), and 100 mg of NaCl flux.

**Synthesis of  $\text{Ba}_2\text{Gd}_{1-x}\text{Mn}_2\text{Te}_5$ .** Black irregular shaped crystals of  $\text{Ba}_2\text{Gd}_{1-x}\text{Mn}_2\text{Te}_5$  (Ba : Gd : Mn : Te in 9.5 : 19 : 10 : 48 ratio) were obtained from the reaction mixtures of Ba (11.9 mg, 0.087 mmol), Gd (27.2 mg, 0.173 mmol), Mn (5.0 mg, 0.091 mmol), and Te (55.8 mg, 0.438 mmol) in 100 mg of NaCl that acted as a molten flux.

**Synthesis of  $\text{Ba}_2\text{Yb}_{1-x}\text{Mn}_2\text{Te}_5$ .** Black crystals of  $\text{Ba}_2\text{Yb}_{1-x}\text{Mn}_2\text{Te}_5$  (Ba : Yb : Mn : Te in 6 : 2 : 6 : 15 ratio) were obtained from the reaction mixtures of Ba (24.1 mg, 0.176 mmol), Yb (10.1 mg, 0.058 mmol), Mn (9.6 mg, 0.176 mmol), and Te (56.1 mg, 0.439 mmol) in 100 mg of NaCl used as a flux.

The energy dispersive X-ray spectroscopic (EDS) method was employed to analyze the elemental compositions of the reaction products using the octane elite energy dispersive X-ray spectrometer (EDAX Inc., USA) attached to the field-emission scanning electron microscope (FE-SEM) (make: JEOL, Japan; model: JSM 7800F). The EDS data were collected with an accelerating voltage of 15–20 kV. The sizes of the crystals obtained

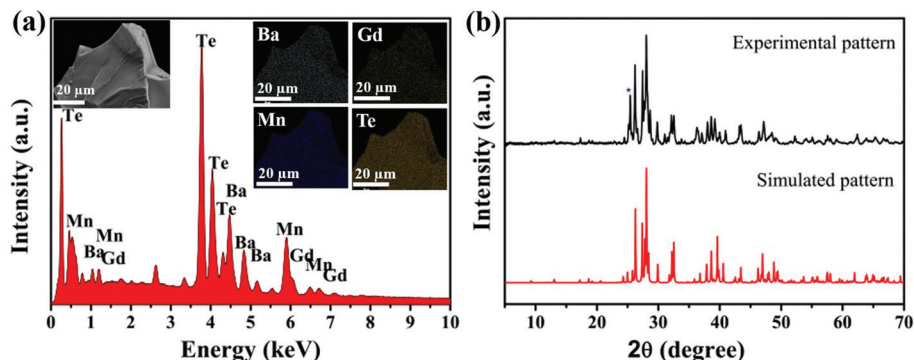


**Fig. 1** (a) The EDS mapping and point analysis of  $\text{Ba}_{2.03(2)}\text{Gd}_{0.66(5)}\text{Mn}_{2.07(4)}\text{Te}_{5.11(6)}$  crystals and (b) the PXRD pattern of the polycrystalline  $\text{Ba}_2\text{Gd}_{2/3}\text{Mn}_2\text{Te}_5$  compound. The asterisk indicates the reflection from the secondary BaTe phase.

from the reactions were in the range of  $\sim 20\ \mu\text{m}$ – $200\ \mu\text{m}$ . A few crystals were selected from the reaction products and placed on carbon tape affixed to a stub. The EDS data were collected on these crystals. Some of the black crystals showed four elements, Ba, Ln, Mn, and Te, using a semiquantitative EDS analysis. The composition of these black crystals was close to  $\text{Ba}_2\text{Ln}_{2/3}\text{Mn}_2\text{Te}_5$  composition. The EDS mapping of a typical crystal of Gd-compound (shown in Fig. 1(a)) shows the homogeneous distribution of all four elements consistent with  $\text{Ba}_{2.03(2)}\text{Gd}_{0.66(5)}\text{Mn}_{2.07(4)}\text{Te}_{5.11(6)}$  composition. Our EDS study did not detect any trace of sodium/chlorine/silicon in the black crystals of  $\text{Ba}_2\text{Ln}_{1-x}\text{Mn}_2\text{Te}_5$ . These crystals were carefully removed from the carbon tape after the EDS studies and used for single crystal diffraction studies.

**2.1.2. Syntheses of polycrystalline  $\text{Ba}_2\text{Ln}_{2/3}\text{Mn}_2\text{Te}_5$ .** After establishing the composition and crystal structure of  $\text{Ba}_2\text{Ln}_{2/3}\text{Mn}_2\text{Te}_5$ , polycrystalline samples of these quaternary phases were synthesized using the sealed tube solid-state method. A stoichiometric amount of Ba, Ln, Mn, and Te was loaded inside a carbon-coated fused silica tube having 10 mm inner diameter and 12 mm outer diameter inside an argon filled glove box. The total mass of the reactants was about 400 mg in each reaction. The fused silica tube containing the reaction mixture was first evacuated (*ca.*  $10^{-4}$  Torr) and sealed using a flame torch. The sealed ampoule was then placed inside a programmable muffle furnace, and the temperature was ramped up to 1273 K with a heating rate of  $\sim 78\ \text{K h}^{-1}$ . The reaction mixture was annealed at 1273 K for 120 h before the furnace was switched off and allowed to cool to room temperature. The reaction tube was opened under ambient conditions to reveal a homogeneous looking black product that was further ground into fine powder inside the argon-filled glove box. The powder X-ray diffraction data of this black polycrystalline product were collected for phase identification.

## 2.2. Single-crystal X-ray diffraction

Single-crystal X-ray diffraction data of  $\text{Ba}_2\text{Gd}_{1-x}\text{Mn}_2\text{Te}_5$  were collected at 298(2) K using a Rigaku Supernova X-Calibur equipped with an Eos CCD detector with a graphite monochromatic Mo-K $\alpha$  radiation ( $\lambda = 0.71073\ \text{\AA}$ ). The black irregular-

shaped crystals subjected to the EDS study were first placed on a glass slide under Paratone-N oil. The unit cell determinations of few crystals were performed to ascertain the quality of these crystals. A suitable sized single crystal was then mounted on a KM4/Xcalibur Goniometer. The crystal-to-detector distance was fixed at 45 mm and an exposure time of 20 s per frame was used for data collection in a series of  $0.6^\circ$  in  $\omega$  scans. The CrysAlis<sup>PRO</sup> program<sup>26</sup> was used to collect intensity data, cell refinement, and data reduction. The absorption corrections of the measured intensities of the reflections were performed by the multi-scan method using the SCALE3 ABSPACK.<sup>27</sup>

Room temperature (298(2) K) single-crystal X-ray diffraction data of  $\text{Ba}_2\text{Ln}_{1-x}\text{Mn}_2\text{Te}_5$  (Ln = Pr and Yb) crystals were recorded using a Bruker D8 Venture instrument equipped with a Photon III mixed mode detector. A graphite monochromatized Mo-K $\alpha$  radiation with a wavelength of  $0.71073\ \text{\AA}$  was used to collect the data. The EDS analyzed crystals were picked under paratone oil for unit cell determination. A suitable crystal was chosen on the goniometer head to collect the data. The working voltage and operating currents were 50 kV and 1.4 mA, respectively, throughout the experiment. The detector to crystal distance was fixed at 50 mm, and an exposure time of 2 s per frame was used for data collection. The data were collected as a series of  $0.5^\circ$  frame width  $\omega$  and  $\phi$  scans. The data collection, cell refinement, and data reduction were carried out with the help of APEX3 software.<sup>28</sup> The absorption corrections were done by the multi-scan method using SADABS.<sup>29</sup>

The crystal structures of  $\text{Ba}_2\text{Ln}_{1-x}\text{Mn}_2\text{Te}_5$  (Ln = Pr, Gd, and Yb) were solved using the SHELX-14 suite programs.<sup>30</sup> The XPREP program<sup>31</sup> suggested monoclinic symmetry with the *C*-centering of the cell and indicated three possible space groups (*C*2, *C*2/*m*, and *C**m*) consistent with the observed reflections' extinction condition. The statistical intensity ( $|E^2 - 1|$ ) value indicated a centrosymmetric structure. Hence, a centrosymmetric monoclinic *C*2/*m* (no. 12) space group was used for the structure solution. The crystal structure's initial model was obtained by the direct methods using the SHELXS program<sup>32</sup> that identified six crystallographic independent atomic positions. These sites were modeled with one manganese, one

lanthanide, one barium, and three tellurium positions as per their coordination environments and interatomic distances. The isotropic thermal parameters of the Ln atoms in all three structures were relatively larger. The Ln site's occupancy refinement reveals that this site is partially vacant, with a site occupancy factor close to 65–68% for Pr–Gd structures and about 74% for the Yb-structure. Further occupancy refinements of the Ln sites lead to a reduction in the  $R(F)/R_w(F_o^2)$  values. The occupancy refinements of Ba sites in these three structures did not show any vacancy when refined freely while keeping all the other atomic sites fixed to unity. However, for Pr and Gd structures, simultaneous refinements of site occupancy factors (sof) of Ba and Ln sites show vacancy at the Ba sites as well (about 90–92%). The occupancy refinement results were dependent on whether one varied the occupancies of Ba and Ln sites while fixing the occupancies of Mn, and three Te sites as one (*i.e.*, 100%) or whether one varied the occupancies of Ba, Mn, Te1, Te2, and, Te3 while keeping the occupancy of Ln fixed. The agreement factors [ $R(F)/R_w(F_o^2)$ ] were found to be a minimum when occupancies of all sites were freely refined. However, the resulting compositions did not charge balance. It should be noted that the vacancy at the Ba site along with the vacant Pr/Gd sites is not expected as it will result in an overall negative charge on these compounds. It is well known that in many cases, the refinement of X-ray occupancies is not reliable and can have large errors associated with it, especially in the crystals with high X-ray mass absorption coefficients. In such cases, the refinements can be stable and converge to a false minimum. Furthermore, charge balancing in Pr and Gd compounds requires one-third (~33%) of the Ln sites to be unoccupied if all the other sites are completely filled. The refined occupancies of the Pr/Gd sites were indeed close to 65–68%. Hence, instead of reporting the refined compositions as  $Ba_{2-y}Ln_{1-x}Mn_2Te_5$ , we have fixed the Ln sites' occupancies to 2/3 (*i.e.*, 0.6667) in the final cycles of least square refinements to achieve charge neutrality, which leads to  $Ba_2Ln_{2/3}Mn_2Te_5$  (Ln = Pr and Gd) compositions with two formula units (Z) per cell of the structure. For the  $Ba_2Yb_{1-x}Mn_2Te_5$  structure, the refined occupancies of Ba and Yb sites were found to be close

to 100% and ~74%, respectively. We found that the refined occupancy values of Ba and Yb sites were very close when we varied the occupancies of Ba and Yb together or when Yb was fixed and Ba was free and *vice versa*. Ytterbium is well known for exhibiting a mixed valence state (+2/+3) in solid-state compounds, and hence we have not fixed the occupancy of the Yb site during the final cycles of the structure refinements. The final refined formula for the Yb compound is  $Ba_2Yb_{0.74(1)}Mn_2Te_5$ .

To show the atomic vacancy at the Pr/Gd site, the general chemical formula of Pr and Gd-based quaternary compounds will now be referred to as  $Ba_2Ln_{2/3}\square_{1/3}Mn_2Te_5$  (Ln = Pr and Gd;  $\square$  = vacancy at Ln sites) in this article. The precession images of the single crystal-data did not show the presence of any superstructure/satellite reflections. Finally, the parameters like scale factors, atomic positions with anisotropic displacement parameters, and extinction parameters were refined. The final structure was run through the ADDSYM program<sup>33</sup> of PLATON<sup>33</sup> that shows no missing symmetry. The atomic positions were finally standardized using the program STRUCTURE TIDY.<sup>34</sup> Further details are given in Tables 1–3.

### 2.3. Powder X-ray diffraction (PXRD) study

The phase purity of the polycrystalline reaction products was evaluated by PXRD studies. The PXRD data of the finely ground samples were collected at room temperature using a Rigaku Ultima IV diffractometer with a Cu-K $\alpha$  radiation ( $\lambda = 1.5406 \text{ \AA}$ ) source. The PXRD data were recorded over a  $2\theta$  range of  $5^\circ$  to  $70^\circ$  using a  $\theta$ - $2\theta$  geometry. The experimental PXRD patterns were compared with the calculated PXRD patterns simulated from the single-crystal structural data. The presence/absence of a secondary phase(s) was established by the phase analysis of the PXRD patterns using the Match3! Software.<sup>35</sup>

### 2.4. UV-visible-near infrared (UV-vis-NIR) absorption study

The optical bandgap study of  $Ba_2Gd_{2/3}\square_{1/3}Mn_2Te_5$  was carried out at room temperature (298(2) K). A polycrystalline  $Ba_2Gd_{2/3}\square_{1/3}Mn_2Te_5$  sample was homogenized into a fine

**Table 1** Crystallographic data and structural refinement details of  $Ba_2Ln_{1-x}Mn_2Te_5$  structures<sup>a</sup>

Chemical formula	$Ba_2Pr_{2/3}\square_{1/3}Mn_2Te_5$	$Ba_2Gd_{2/3}\square_{1/3}Mn_2Te_5$	$Ba_2Yb_{0.74(1)}Mn_2Te_5$
Space group		$C2/m$	
$a$ (Å)	15.268(3)	15.246(3)	15.266(3)
$b$ (Å)	4.5817(9)	4.5479(9)	4.5784(9)
$c$ (Å)	10.737(2)	10.688(2)	10.664(2)
$\beta^\circ$	117.23(3)	117.20(3)	116.92(3)
$V$ (Å <sup>3</sup> )	667.8(3)	659.1(3)	664.6(3)
Z		2	
$\rho$ (g cm <sup>-3</sup> )	5.551	5.681	5.754
$\mu$ (mm <sup>-1</sup> )	20.68	21.85	23.58
$R(F)^b$	0.032	0.0296	0.028
$R_w(F_o^2)^c$	0.081	0.0742	0.067

<sup>a</sup>  $\lambda = 0.71073 \text{ \AA}$ ,  $T = 298(2) \text{ K}$ . <sup>b</sup>  $R(F) = \sum ||F_o| - |F_c|| / \sum |F_o|$  for  $F_o^2 > 2\sigma(F_o^2)$ . <sup>c</sup>  $R_w(F_o^2) = \{ \sum [w(F_o^2 - F_c^2)^2] / \sum wF_o^4 \}^{1/2}$ . For  $F_o^2 < 0$ ,  $w = 1 / [\sigma^2(F_o^2) + (rP)^2 + mP]$  where  $P = (F_o^2 + 2F_c^2) / 3$ , ( $r = 0.0199$  and  $m = 22.5849$  for  $Ba_2Pr_{2/3}\square_{1/3}Mn_2Te_5$ ,  $r = 0.0158$  and  $m = 30.3751$  for  $Ba_2Gd_{2/3}\square_{1/3}Mn_2Te_5$ , and  $r = 0.0107$  and  $m = 13.0832$  for  $Ba_2Yb_{0.74(1)}Mn_2Te_5$ ).

**Table 2** Fractional atomic coordinates and  $U_{\text{iso}}/U_{\text{eq}}$  values of  $\text{Ba}_2\text{Ln}_{1-x}\text{Mn}_2\text{Te}_5$  structures

Atoms	Wyckoff position	Site symmetry	S.O.F.	<i>x</i>	<i>y</i>	<i>z</i>	$U_{\text{iso}}/U_{\text{eq}}^a$
<b><math>\text{Ba}_2\text{Pr}_{2/3}\square_{1/3}\text{Mn}_2\text{Te}_5</math></b>							
Ba1	4 <i>i</i>	<i>m</i>	1	0.17486(4)	0.000000	0.72576(7)	0.02645(18)
Pr1	2 <i>a</i>	2/ <i>m</i>	2/3	0.000000	0.000000	0.000000	0.0204(2)
Mn1	4 <i>i</i>	<i>m</i>	1	0.56260(11)	0.000000	0.30161(15)	0.0214(3)
Te1	4 <i>i</i>	<i>m</i>	1	0.16438(5)	0.000000	0.31604(7)	0.02503(18)
Te2	4 <i>i</i>	<i>m</i>	1	0.38396(4)	0.000000	0.06589(6)	0.01964(16)
Te3	2 <i>d</i>	2/ <i>m</i>	1	0.000000	0.500000	0.500000	0.01895(19)
<b><math>\text{Ba}_2\text{Gd}_{2/3}\square_{1/3}\text{Mn}_2\text{Te}_5</math></b>							
Ba1	4 <i>i</i>	<i>m</i>	1	0.17437(5)	0.000000	0.72809(8)	0.02680(2)
Gd1	2 <i>a</i>	2/ <i>m</i>	2/3	0.000000	0.000000	0.000000	0.01980(2)
Mn1	4 <i>i</i>	<i>m</i>	1	0.56300(12)	0.000000	0.30167(18)	0.02050(3)
Te1	4 <i>i</i>	<i>m</i>	1	0.16410(5)	0.000000	0.31200(8)	0.02320(2)
Te2	4 <i>i</i>	<i>m</i>	1	0.38556(5)	0.000000	0.06390(7)	0.01848(18)
Te3	2 <i>d</i>	2/ <i>m</i>	1	0.000000	0.500000	0.500000	0.01820(2)
<b><math>\text{Ba}_2\text{Yb}_{0.74(1)}\text{Mn}_2\text{Te}_5</math></b>							
Ba1	4 <i>i</i>	<i>m</i>	1	0.17538(3)	0.000000	0.72820(5)	0.02135(12)
Yb1	2 <i>a</i>	2/ <i>m</i>	0.745(3)	0.000000	0.000000	0.000000	0.01950(19)
Mn1	4 <i>i</i>	<i>m</i>	1	0.56160(8)	0.000000	0.29775(12)	0.0198(3)
Te1	4 <i>i</i>	<i>m</i>	1	0.16387(4)	0.000000	0.31528(6)	0.02327(13)
Te2	4 <i>i</i>	<i>m</i>	1	0.38440(3)	0.000000	0.06434(5)	0.02029(13)
Te3	2 <i>d</i>	2/ <i>m</i>	1	0.000000	0.500000	0.500000	0.01898(15)

<sup>a</sup>  $U_{\text{iso}}/U_{\text{eq}}$  is the one-third value of the trace of orthogonalized  $U_{ij}$  tensor.

**Table 3** Selected interatomic distances (Å) of  $\text{Ba}_2\text{Ln}_{1-x}\text{Mn}_2\text{Te}_5$  structures

Atomic pair	$\text{Ba}_2\text{Pr}_{2/3}\square_{1/3}\text{Mn}_2\text{Te}_5$	$\text{Ba}_2\text{Gd}_{2/3}\square_{1/3}\text{Mn}_2\text{Te}_5$	$\text{Ba}_2\text{Yb}_{0.74(1)}\text{Mn}_2\text{Te}_5$
Ln1–Te1	3.1654(15) × 2	3.1229(16) × 2	3.1539(14) × 2
Ln1–Te2	3.1676(6) × 4	3.1258(6) × 4	3.1498(6) × 4
Mn1–Te1	2.7325(9) × 2	2.7209(11) × 2	2.7292(8) × 2
Mn1–Te2	2.744(2)	2.7371(22)	2.7233(17)
Mn1–Te3	2.7043(15)	2.6975(17)	2.7153(12)
Ba1–Te1	3.5329(8) × 2	3.5190(9) × 2	3.5366(7) × 2
Ba1–Te2	3.5861(18)	3.5616(19)	3.5602(17)
Ba1–Te2	3.5913(8) × 2	3.5784(9) × 2	3.5772(7) × 2
Ba1–Te3	3.5114(11) × 2	3.5010(11) × 2	3.5258(10) × 2
Ba1...Ba1	4.582(1)	4.548(1)	4.578(1)
Ba1...Ln1	4.792(1)	4.751(1)	4.753(1)
Ba1...Mn1	4.151(1)	4.159(1)	4.148(1)
Ln1...Mn1	3.717(1)	3.696(1)	3.674(1)
Ln1...Ln1	4.582(1)	4.548(1)	4.578(1)
Mn1...Mn1	4.582(1)	4.548(1)	4.578(1)
Te1...Te1	4.270(1)	4.308(1)	4.277(1)
Te1...Te2	4.454(1)	4.371(1)	4.413(1)
Te1...Te3	4.470(1)	4.479(1)	4.454(1)
Te2...Te2	4.323(1)	4.289(1)	4.327(1)
Te2...Te3	4.160(1)	4.163(1)	4.156(1)
Te3...Te3	4.582(1)	4.548(1)	4.578(1)

powder inside an Ar-filled glove box. The absorption study was then performed against dried  $\text{BaSO}_4$  powder, which served as a standard reference for the UV-vis-NIR absorption study. A JASCO V-770 UV/vis/NIR spectrometer was used to collect the data in diffuse reflectance mode over the wavelength range of 2000 nm (0.62 eV) to 250 nm (4.96 eV). The Kubelka–Munk equation,  $\alpha/S = (1 - R)^2/2R$ , was used to transform the reflectance data into absorption data. Here  $\alpha$ ,  $S$ , and  $R$  are the absorption coefficient, scattering coefficient, and reflectance, respectively.<sup>36</sup> The absorption vs. energy plot was used to estimate the bandgap by absorption edge study.

## 2.5. Temperature-dependent resistivity study

The temperature-dependent four-probe resistivity data were collected for a sintered polycrystalline rectangular pellet of  $\text{Ba}_2\text{Gd}_{2/3}\square_{1/3}\text{Mn}_2\text{Te}_5$  over a temperature range of 95–300 K. A polycrystalline sample of  $\text{Ba}_2\text{Gd}_{2/3}\square_{1/3}\text{Mn}_2\text{Te}_5$  was compressed into a cylindrical disk with a diameter of 8 mm and a thickness of  $\approx 3$  mm under a pressure of  $\approx 10$  MPa. The pellet was placed inside a carbon-coated fused silica tube and vacuum-sealed using a flame torch. The sealed pellet was sintered at 673 K for 24 hours. Finally, the cylindrical pellet was cut into a

rectangular pellet for resistivity measurement. The procedure and the equipment details are the same as we described previously.<sup>37</sup>

## 2.6. Temperature-dependent magnetic measurements

Magnetization ( $M$ ) measurements of polycrystalline samples of  $\text{Ba}_2\text{Gd}_{2/3}\square_{1/3}\text{Mn}_2\text{Te}_5$  were obtained using a Quantum Design Physical Properties Measurement System (PPMS). The temperature-dependent magnetization data were collected in the zero-field cooling (ZFC) mode (5 K–300 K) and field cooling (FC) mode (300 K–5 K) under an applied magnetic field ( $H$ ) of 1000 Oe.

## 2.7. Electronic structure calculations

The *ab initio* quantum mechanical calculations are performed using the plane-wave basis set formalism within the framework of density functional theory (DFT)<sup>38</sup> as implemented in the VASP Package.<sup>39</sup> The interactions between the core and valence electrons are approximated using the projected augmented wave (PAW) potentials.<sup>40</sup> In the case of Mn atoms, the 3p semicore states are treated as valence states. The GGA+U approach<sup>41</sup> is used to include the on-site correlations for the Mn-3d orbitals. For Gd atoms, the localized 4f states and semicore 3p states are treated as the core states and valence states, respectively. It may be noted that f-electrons are generally not handled well within the DFT framework due to self-interaction errors. However, Gd is described reasonably well as seven electrons occupy the majority f-shell. In the case of Ba atoms, semicore 5s and 5p states are treated as valence states. The exchange–correlation effects are treated using the Perdew–Burke–Ernzerhoff (PBE)<sup>42</sup> form of generalized gradient approximation (GGA). A kinetic energy cutoff of a minimum of 300 eV is used to expand the Kohn–Sham orbitals in the plane-wave basis set. The integrations in the  $k$ -space are performed by sampling the Brillouin zone using a  $6 \times 6 \times 8$  Monkhorst–Pack  $k$ -point mesh. The lattice parameters and the fractional coordinates of the atoms in the unit cell are relaxed until the Hellmann–Feynman forces become less than  $30 \text{ meV } \text{\AA}^{-1}$ . Self-consistency in calculations is achieved with total energies converging up to  $10^{-5}$  eV per cell. The unit cell of  $\text{Ba}_2\text{Gd}_{2/3}\square_{1/3}\text{Mn}_2\text{Te}_5$  contains two formula units ( $Z = 2$ ), which correspond to  $\text{Ba}_4\text{Gd}_{4/3}\square_{2/3}\text{Mn}_4\text{Te}_{10}$ . The fractional occupancy of a Gd atom in the  $(1 \times 1 \times 1)$  one-unit cell with the  $\text{Ba}_4\text{Gd}_{4/3}\square_{2/3}\text{Mn}_4\text{Te}_{10}$  composition is modeled using a larger  $(1 \times 3 \times 1)$  unit cell with 2 Gd atoms and one vacancy per unit cell, *i.e.*, the  $\text{Ba}_6\text{Gd}_2\square\text{Mn}_6\text{Te}_{15}$  composition.

# 3. Results and discussion

## 3.1. Syntheses and crystal structures of $\text{Ba}_2\text{Ln}_{1-x}\text{Mn}_2\text{Te}_5$ (Ln = Pr, Gd, and Yb)

The black-colored crystals of these new quaternary compounds were first synthesized by the solid-state reactions of elements at 1273 K using an excess of NaCl molten flux. The approximate yields of  $\text{Ba}_2\text{Ln}_{2/3}\square_{1/3}\text{Mn}_2\text{Te}_5$  (Ln = Pr and Gd) and

$\text{Ba}_2\text{Yb}_{0.74(1)}\text{Mn}_2\text{Te}_5$  crystals were about 20% to 40% based on the manganese. The use of NaCl flux is essential for the growth of the crystals since the corresponding flux-free reactions only produced mixtures of polycrystalline products. Attempts towards synthesizing  $\text{Ba}_2\text{Ln}_{1-x}\text{Mn}_2\text{Te}_5$  (Ln = La, Ce, Nd, and Sm) crystals failed, and only crystals of  $\text{Ba}_2\text{MnTe}_3$ <sup>43</sup> and respective binary lanthanum telluride phases were observed in their final reaction products. A series of stoichiometric flux free solid-state reactions of Ba, Ln, Mn, and Te elements were carried out with varying temperature profiles to optimize the reaction conditions and to obtain monophasic polycrystalline samples of  $\text{Ba}_2\text{Ln}_{1-x}\text{Mn}_2\text{Te}_5$ . Most of these reactions produced the target phase as a minor phase along with known ternary and binary phases [see the ESI†]. Only for the Gd compound, *i.e.*,  $\text{Ba}_2\text{Gd}_{2/3}\square_{1/3}\text{Mn}_2\text{Te}_5$ , the target phase was obtained as the main phase along with small amounts of BaTe as a secondary phase (Fig. 1b). This polycrystalline sample of  $\text{Ba}_2\text{Gd}_{2/3}\square_{1/3}\text{Mn}_2\text{Te}_5$  was obtained by the stoichiometric reaction of the corresponding elements at 1273 K. The reactants were heated at 1273 K for five days to produce a black lump that was homogenized and used for further characterization.

**3.1.1. Crystal structures of  $\text{Ba}_2\text{Ln}_{1-x}\text{Mn}_2\text{Te}_5$  (Ln = Pr, Gd, and Yb).** Single-crystal X-ray diffraction studies at 298(2) K were used to establish the crystal structures of these three quaternary compounds. These compounds crystallize in the monoclinic  $C_{2h}^3 - C2/m$  space group with two formula units per cell. The refined cell constants for  $\text{Ba}_2\text{Pr}_{2/3}\square_{1/3}\text{Mn}_2\text{Te}_5$  are  $a = 15.268(3) \text{ \AA}$ ,  $b = 4.5817(9) \text{ \AA}$ ,  $c = 10.737(2) \text{ \AA}$ , and  $\beta = 117.23(3)^\circ$ . The lattice parameters of  $\text{Ba}_2\text{Ln}_{2/3}\square_{1/3}\text{Mn}_2\text{Te}_5$  were observed to decrease with the substitution of smaller Gd atoms (Table 1). The observed reduction in the lattice parameters is consistent with lanthanide contraction. However, the refined  $a$  and  $b$ -lattice constants and cell volume for the Yb compound are slightly larger than those observed for the Gd compound. This could be due to the mixed valency of Yb (+2/+3) species. These structures can be viewed as a defect variant of the  $\text{Ba}_2\text{UCu}_2\text{S}_5$  structure type (space group:  $C2/m$ ).<sup>44</sup> The asymmetric unit of the  $\text{Ba}_2\text{Ln}_{1-x}\text{Mn}_2\text{Te}_5$  (Ln = Pr, Gd, and Yb) structure comprises six independent crystallographic sites: one Ba1, one Ln1, one Mn1, and three Te sites (Te1, Te2, and Te3). All the atomic sites have a site symmetry of  $.m$  except for Ln1 and Te3 that occupy the sites with  $.2/m$  symmetry. All these crystallographic sites are fully occupied except for the Ln1 site. Only two-thirds of the Ln site is filled for Pr and Gd-compounds, leaving one-third of the Pr1/Gd1 sites unoccupied. For  $\text{Ba}_2\text{Yb}_{0.74(1)}\text{Mn}_2\text{Te}_5$ , the Yb site occupancy is about 74%, slightly larger than the Pr/Gd compounds. The site symmetries and Wyckoff positions of these atoms are listed in Table 2. The overall crystal structure of these three compounds can be described as pseudo-two dimensional, as shown in Fig. 2. Each Ln atom in this structure is located at the center of a distorted octahedron formed by two Te1 and four Te2 atoms. In contrast, Mn atoms are bound to four Te atoms ( $2 \times \text{Te1}$ ,  $1 \times \text{Te2}$ , and  $1 \times \text{Te3}$ ) in a tetrahedral fashion.

The Pr–Te bond distances in  $\text{Ba}_2\text{Pr}_{2/3}\square_{1/3}\text{Mn}_2\text{Te}_5$  range from  $3.165(2) \text{ \AA}$  to  $3.168(1) \text{ \AA}$  which are in good agreement

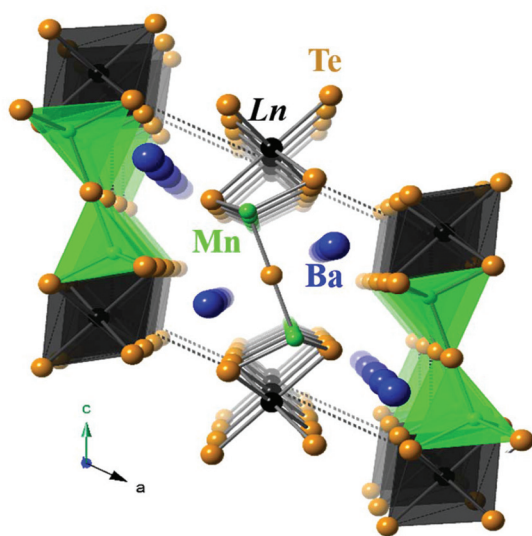


Fig. 2 A unit cell view of the  $\text{Ba}_2\text{Ln}_{1-x}\text{Mn}_2\text{Te}_5$  crystal structures along the [010] direction.

with the  $\text{Pr}^{3+}$ -Te distances in  $\text{CsPrCdTe}_3$  (3.192(2) Å to 3.195(2) Å),<sup>21</sup>  $\text{CsPrZnTe}_3$  (3.1394(4) Å to 3.1616(4) Å),<sup>45</sup>  $\text{PrCu}_{0.45(1)}\text{Te}_2$  (3.150(1) Å to 3.3175(7) Å),<sup>46</sup> and  $\text{CsPr}_2\text{Ag}_3\text{Te}_5$  (3.151(2) Å to 3.223(2) Å).<sup>47</sup> The Gd-Te bond distances of 3.123(2) Å to 3.126(1) Å in the  $\text{Ba}_2\text{Gd}_{2/3}\text{Mn}_2\text{Te}_5$  structure are somewhat shorter than the Pr-analogue due to the smaller size of  $\text{Gd}^{3+}$  relative to the  $\text{Pr}^{3+}$  ion.<sup>48</sup> The  $\text{Gd}^{3+}$ -Te distances are comparable to those observed in related structures such as  $\text{CsZnGdTe}_3$  (3.0859(3) Å to 3.1025(3) Å)<sup>45</sup> and  $\text{CsCdGdTe}_3$  (3.130(1) Å to 3.144(1) Å).<sup>21</sup>

The Yb-Te bond distances of 3.150(1) Å to 3.154(2) Å in  $\text{Ba}_2\text{Yb}_{0.74(1)}\text{Mn}_2\text{Te}_5$  are slightly longer than the corresponding distances in the Gd compound. The chemistry of ytterbium-based tellurides is relatively less explored, resulting in very few known compounds.<sup>24</sup> To the best of our knowledge, there are only two known examples of Yb containing quaternary tellurides:  $\text{RbYbZnTe}_3$  and  $\text{CsYbZnTe}_3$ .<sup>22</sup> These two tellurides contain ytterbium in the +3 oxidation state, and the coordination environments around the Yb atoms are also octahedral. The ionic size of  $\text{Yb}^{2+}$  (1.02 Å) with a six coordination number is larger than the  $\text{Yb}^{3+}$  (0.868 Å).<sup>48</sup> Thus, it is expected that the  $\text{Yb}^{2+}$ -Te distances will be longer than the  $\text{Yb}^{3+}$ -Te in similar coordination environments. The  $\text{Yb}^{3+}$ -Te distances found in  $\text{RbYbZnTe}_3$  (3.0264(4) Å to 3.0501(4) Å)<sup>22</sup> and  $\text{CsYbZnTe}_3$  (3.0328(6) Å to 3.0417(5) Å)<sup>22</sup> are indeed slightly shorter than the Yb-Te bond distances in  $\text{Ba}_2\text{Yb}_{0.74(1)}\text{Mn}_2\text{Te}_5$ .

One of the most stable tellurides of ytterbium is cubic  $\text{YbTe}$  (space group:  $Fm\bar{3}m$ ), where divalent ytterbium is present.<sup>49</sup> The coordination environment around the Yb atom in  $\text{YbTe}$  is octahedral with six equal  $\text{Yb}^{2+}$ -Te bond distances of 3.185(1) Å. These distances are slightly longer than those observed in  $\text{Ba}_2\text{Yb}_{0.74(1)}\text{Mn}_2\text{Te}_5$ . The Yb-Te distance in ternary phase  $\text{YbGa}_6\text{Te}_{10}$  (Yb is ~65% occupied), which adopts the filled beta-manganese structure, varies from 3.180(1) Å to 3.260(1)

Å.<sup>50</sup> The coordination geometry around the Yb atom in  $\text{YbGa}_6\text{Te}_{10}$  is severely distorted octahedral, and the oxidation state of ytterbium is reported as +2 based on the crystal structure refinement results. The  $\text{Yb}^{2+}$ -Te distances in  $\text{YbGa}_6\text{Te}_{10}$  are also slightly longer than the Yb-Te distances observed in our quaternary compound. Thus, based on the comparison of the Yb-Te distances in  $\text{Ba}_2\text{Yb}_{0.74(1)}\text{Mn}_2\text{Te}_5$  with the related structures, a mixed valency of Yb (+2/+3) is expected in  $\text{Ba}_2\text{Yb}_{0.74(1)}\text{Mn}_2\text{Te}_5$ . However, detailed X-ray photoelectron spectroscopy and magnetic studies are needed to support this conjecture. Regrettably, we could not synthesize either bigger crystals or a single-phase polycrystalline  $\text{Ba}_2\text{Yb}_{0.74(1)}\text{Mn}_2\text{Te}_5$  for such measurements. We have obtained a mixture of polycrystalline  $\text{YbTe}$ ,<sup>49</sup>  $\text{Ba}_2\text{MnTe}_3$ ,<sup>43</sup> and the target phase in the reaction aimed for the synthesis of bulk  $\text{Ba}_2\text{Yb}_{1-x}\text{Mn}_2\text{Te}_5$  (see the ESI†).

The Mn-Te bond distances of 2.697(2) Å to 2.744(2) Å in the tetrahedral units of  $\text{MnTe}_4$  of  $\text{Ba}_2\text{Ln}_{1-x}\text{Mn}_2\text{Te}_5$  are in fair agreement with the  $\text{Mn}^{2+}$ -Te distances reported in related structures with Mn in tetrahedral coordination. Examples include  $\text{CsMnInTe}_3$  (Mn<sup>2+</sup>-Te distances of 2.707(2) to 2.771(2) Å),<sup>51</sup>  $\text{Ba}_2\text{MnTe}_3$  (2.640(1) to 2.733(1) Å),<sup>43</sup> and  $\text{Cs}_2\text{Mn}_3\text{Te}_4$  (2.7379(7) to 2.7515(8) Å).<sup>52</sup>

Based on the coordination geometries of the Ln and Mn atoms, the building blocks of the  $\text{Ba}_2\text{Ln}_{1-x}\text{Mn}_2\text{Te}_5$  structures (Ln = Pr, Gd, and Yb) could be assigned to the  $\text{LnTe}_6$  octahedra and  $\text{MnTe}_4$  tetrahedra. Each  $\text{LnTe}_6$  octahedron is connected to two neighboring  $\text{LnTe}_6$  units by sharing two opposite edges along the *b*-axis to form infinite chains of  $[\text{Ln}_{1-x}\text{Te}_4]^{6-}$ . These  $[\text{Ln}_{1-x}\text{Te}_4]^{6-}$  chains are missing one-third and about 26% of Pr/Gd and Yb atoms, respectively, on average. Three membered linear units of Mn1-Te3-Mn1 link two neighboring chains of  $[\text{Ln}_{1-x}\text{Te}_4]^{6-}$  to form infinite layers of  ${}_{\infty}^2[\text{Ln}_{1-x}\text{Mn}_2\text{Te}_5]^{4-}$  as shown in Fig. 3(a). The infinite layers of  ${}_{\infty}^2[\text{Ln}_{1-x}\text{Mn}_2\text{Te}_5]^{4-}$  are separated by the  $\text{Ba}^{2+}$  cations. Each  $\text{MnTe}_4$  tetrahedron in this structure is connected to three neighboring  $\text{MnTe}_4$  tetrahedra *via* the sharing of two vertices ( $2 \times \text{Te}1$ ) along the *b*-axis and one vertex (Te3) roughly along the *c*-axis. Finally, the Ln-based octahedra and Mn-based tetrahedra are joined *via* edge-sharing in the infinite layers of  ${}_{\infty}^2[\text{Ln}_{1-x}\text{Mn}_2\text{Te}_5]^{4-}$ . The  $\text{LnTe}_6$  and  $\text{MnTe}_4$  based polyhedral networks of the  ${}_{\infty}^2[\text{Ln}_{1-x}\text{Mn}_2\text{Te}_5]^{4-}$  layers are connected along the [001] direction in the.....*oct tet tet oct tet tet*..... fashion.

The Ba atoms in these structures are coordinated with seven Te atoms ( $2 \times \text{Te}1$ ,  $3 \times \text{Te}2$ , and  $2 \times \text{Te}3$ ) that form a distorted monocapped trigonal prism-like geometry (Fig. 3(b)). The interatomic distances of Ba-Te in the monocapped trigonal prism  $\text{BaTe}_7$  vary from 3.501(1) Å to 3.5912(8) Å. These distances are consistent with the previously reported distances of 3.451(1) Å to 3.882(1) Å in  $\text{Ba}_2\text{GaGdTe}_5$ ,<sup>53</sup> 3.393(1) Å to 3.714(1) Å in  $\text{Ba}_2\text{MnTe}_3$ ,<sup>43</sup> and 3.4007(2) Å to 3.6408(3) Å in  $\text{Ba}_2\text{ZnTe}_3$ .<sup>54</sup>

As discussed earlier, the  $\text{Ba}_2\text{Ln}_{1-x}\text{Mn}_2\text{Te}_5$  structure can be described as a defect variant of the  $\text{Ba}_2\text{UCu}_2\text{S}_5$  structure.<sup>44</sup> It is derived from the  $\text{Ba}_2\text{UCu}_2\text{S}_5$  structure by the aliovalent substitution of  $\text{Cu}^+$  and  $\text{U}^{4+}$  sites with  $\text{Mn}^{2+}$  and  $\text{Ln}^{3+}$  ions, respectively, and the isovalent substitution of  $\text{S}^{2-}$  sites with

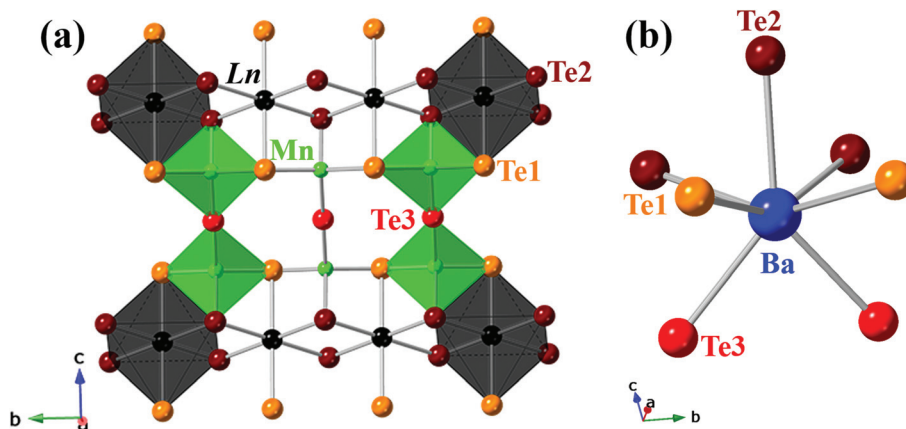


Fig. 3 (a) A segment of the  ${}_{\infty}^2[\text{Ln}_{1-x}\text{Mn}_2\text{Te}_5]^{4-}$  anionic layers and (b) the Ba coordination environment in  $\text{Ba}_2\text{Ln}_{1-x}\text{Mn}_2\text{Te}_5$ .

$\text{Te}^{2-}$ -species. Such a complete substitution of corresponding elements in  $\text{Ba}_2\text{UCu}_2\text{S}_5$  should give a hypothetical  $\text{Ba}_2\text{LnMn}_2\text{Te}_5$  composition. It is apparent that there is a charge-imbalance of +1 in this ideal  $\text{Ba}_2\text{LnMn}_2\text{Te}_5$  composition when all crystallographic sites are fully occupied. To compensate for this extra +1 charge, the  $\text{Pr}^{3+}/\text{Gd}^{3+}$  sites are only two-thirds occupied, which leads to the stabilization of the  $\text{Ba}_2\text{Ln}_{2/3}\square_{1/3}\text{Mn}_2\text{Te}_5$  structure where  $\square$  represents the vacancies at the Ln (= Pr and Gd) sites.

**3.1.2. Assignment of formal oxidation states.** The shortest Te...Te distance of 4.156(1) Å (Table 3) in the  $\text{Ba}_2\text{Ln}_{1-x}\text{Mn}_2\text{Te}_5$  structure implies that there is no bonding interaction between the Te atoms. In addition, this structure type does not show any metal-metal homoatomic bonding. Thus, assignments of formal oxidation states of +2 for Ba and -2 for Te atoms in  $\text{Ba}_2\text{Ln}_{2/3}\square_{1/3}\text{Mn}_2\text{Te}_5$  structures are straightforward. The most stable oxidation state of Pr and Gd is +3. The oxidation of Mn atoms in the  $\text{Ba}_2\text{Ln}_{1-x}\text{Mn}_2\text{Te}_5$  structures could be assigned to +2, the most stable oxidation state known for manganese in the tellurides. Thus, the charge balance can be achieved as  $(\text{Ba}^{2+})_2(\text{Ln}^{3+})_{2/3}(\text{Mn}^{2+})_2(\text{Te}^{2-})_5$  for the Pr and Gd compounds. The charge-balancing in the Yb compound,  $\text{Ba}_2\text{Yb}_{0.74(1)}\text{Mn}_2\text{Te}_5$ , is arbitrary due to the possibility of a mixed-valence state of Yb (+2/+3).

These structures will be electronically unstable if one assumes full Ln site occupancy that corresponds to the  $\text{Ba}_2\text{LnMn}_2\text{Te}_5$  composition. It is apparent that this leads to an overall +1 charge on the  $\text{Ba}_2\text{LnMn}_2\text{Te}_5$  formula for Ln = Pr and Gd. For the Yb compound, the hypothetical  $\text{Ba}_2\text{YbMn}_2\text{Te}_5$  composition will be electronically stable if Yb is only present in the +2 oxidation state. However, the deficiency at the Yb site in this compound indicates a mixed valence state of Yb (+2/+3). Thus, Ln-deficiency stabilizes the  $\text{Ba}_2\text{Ln}_{1-x}\text{Mn}_2\text{Te}_5$  structures electronically. There are many examples known in the literature, where partial occupancy leads to electronic stabilization. For example, stabilization of  $\text{Ba}_{0.5}\text{CuZrSe}_3$ ,<sup>55</sup> which is isostructural to  $\text{CsCuZrSe}_3$ ,<sup>56</sup> requires the replacement of monovalent Cs atoms with half-filled divalent Ba

atoms. It is interesting to note that removing any  $\text{Ln}^{3+}$  species from the Ln sites in the  ${}_{\infty}^2[\text{Ln}_{1-x}\text{Mn}_2\text{Te}_5]^{4-}$  layer will not affect the occupancy of Te atoms since these are all bonded to neighboring Ln and Mn atoms.

**3.1.3. Bond valence sum calculation.** As discussed earlier, the  $\text{Ba}_2\text{Ln}_{2/3}\square_{1/3}\text{Mn}_2\text{Te}_5$  (Ln = Pr and Gd) compounds do not show any homoatomic bonding and hence can be easily charge-balanced based on the Zintl concept with  $2 \times \text{Ba}^{2+}$ ,  $2/3 \times \text{Ln}^{3+}$ ,  $2 \times \text{Mn}^{2+}$ , and  $5 \times \text{Te}^{2-}$ . Furthermore, bond valency sum (BVS) calculations<sup>57,58</sup> for the Pr and Gd-based structures also suggest the same formal charge assignments as discussed above. The complete skeletal structure does not show any distortion even after removing Ln from the structure, which can explain the slightly lower or higher BVS values of Ln and Mn due to their under bonding and over bonding. Although the BVS calculation method is strictly an empirical method, the decrease in the BVS value of lanthanide atoms going from Pr to Yb could be due to the mixed valency of Yb atoms and increased atomic number in a common coordination environment.<sup>59</sup> The more deviation of BVS values in the case of Te3 compared to Te1 and Te2 may be due to its shortest bond length with the metal in the compound's distorted geometry. The BVS details of all the atoms of  $\text{Ba}_2\text{Ln}_{1-x}\text{Mn}_2\text{Te}_5$  compounds are given in Table 4.

### 3.2. Structural relationships of $\text{Ba}_2\text{Ln}_{1-x}\text{Mn}_2\text{Te}_5$ with known related structures

We next discuss the structural commonalities of the  $\text{Ba}_2\text{Ln}_{1-x}\text{Mn}_2\text{Te}_5$  structures with other known related structures found in the quaternary AE-Ln-M-Q system (AE = alkaline-earth; Ln = lanthanides, M = 3d transition metals; Q = chalcogens) and the  $\text{Ba}_2\text{UCu}_2\text{S}_5$  structure type.<sup>44</sup> There are a total of three unique structure types (including  $\text{Ba}_2\text{Ln}_{2/3}\square_{1/3}\text{Mn}_2\text{Te}_5$  structure) known in this quaternary system. The general formulae of these quaternary compounds are  $\text{AELn}_2\text{MQ}_5$  (1215-family) or  $\text{AELnMQ}_3$  (1113-family). The  $\text{AELn}_2\text{MQ}_5$  type compounds crystallize in the  $\text{Cs}_3\text{CoCl}_5$  structure type<sup>60</sup> in the tetragonal space group ( $I4/mcm$ ) and the

Table 4 Bond valency sum (BVS) of atoms in Ba<sub>2</sub>Ln<sub>1-x</sub>Mn<sub>2</sub>Te<sub>5</sub>

	Ba <sub>2</sub> Pr <sub>2/3</sub> □ <sub>1/3</sub> Mn <sub>2</sub> Te <sub>5</sub>	Ba <sub>2</sub> Gd <sub>2/3</sub> □ <sub>1/3</sub> Mn <sub>2</sub> Te <sub>5</sub>	Ba <sub>2</sub> Yb <sub>0.74(1)</sub> Mn <sub>2</sub> Te <sub>5</sub>
Site	BVS	BVS	BVS
Ba1	1.97	2.04	1.98
Ln1	2.92	2.78	2.08
Mn1	2.47	2.53	2.50
Te1	2.30	2.34	2.16
Te2	2.32	2.32	2.12
Te3	2.56	2.62	2.48

AELnMQ<sub>3</sub> type compounds crystallize in two different structure types (structure type: Eu<sub>2</sub>CuS<sub>3</sub>,<sup>61</sup> space group = *Pnma* for Ln = La–Nd; KCuZrS<sub>3</sub>,<sup>62</sup> type with space group *Cmcm* for Ln = Gd–Er) depending upon the size of the Ln<sup>3+</sup> ion. All these compounds have layered structures that are separated by the AE<sup>2+</sup> cations.

The AE atoms in these compounds mainly act as electron donors and are involved in predominantly non-directional ionic bonding. Therefore, these AE<sup>2+</sup> cations are also referred to as space fillers in these structures. The main building blocks of these structures are chalcogen-based polyhedra of lanthanide and transition elements. The coordination geometries of Ln atoms are either octahedral or bicapped trigonal prismatic in these structure types. On the other hand, the transition metals prefer octahedral or tetrahedral coordination geometries.

The structure type, Ba<sub>2</sub>Ln<sub>1-x</sub>Mn<sub>2</sub>Te<sub>5</sub>, shows some resemblance to the well-known layered ALnMTe<sub>3</sub> (A = alkali or alkaline–earth metal; M = transition element; Ln = lanthanides or actinides) structure type (space group *Cmcm*).<sup>8</sup> In both cases, the lanthanide and transition metals form distorted octahedra and distorted tetrahedra by coordinating with six and four Te atoms, respectively. The  ${}_{\infty}[\text{LnMTe}_3]^{n-}$  ( $n = 1$  for alkali and  $n = 2$  for alkaline–earth metal) layers in the ALnMTe<sub>3</sub> structures are separated by electropositive alkali or alkaline earth metals. These A<sup>n+</sup> ( $n = 1$  for alkali and +2 for alkaline–earth) cations are surrounded by eight Te atoms in a bicapped trigonal-prismatic arrangement. In contrast, in Ba<sub>2</sub>Ln<sub>1-x</sub>Mn<sub>2</sub>Te<sub>5</sub>, the Ba

atoms are coordinated by seven Te atoms in a monocapped trigonal prismatic arrangement. The main difference between these two structure types is the sequence of the tetrahedral and octahedral units, as evident in Fig. 4. The ALnMTe<sub>3</sub> structure has the ..*oct tet oct tet oct*.. ordering along the *c*-axis in contrast to the ...*oct tet tet oct*...ordering in Ba<sub>2</sub>Ln<sub>1-x</sub>Mn<sub>2</sub>Te<sub>5</sub> structures.

### 3.3. Optical bandgap study of Ba<sub>2</sub>Gd<sub>2/3</sub>□<sub>1/3</sub>Mn<sub>2</sub>Te<sub>5</sub>

The absorption spectrum of powdered Ba<sub>2</sub>Gd<sub>2/3</sub>□<sub>1/3</sub>Mn<sub>2</sub>Te<sub>5</sub> (Fig. 5) was collected at room temperature (298 (2) K) over a range of 2000 nm to 250 nm wavelength. The optical bandgap of the compound can be deduced by the extrapolation method and was found in the near IR region (~0.86 eV).

To calculate the value of the direct bandgap, we have plotted the Tauc plot that is shown in Fig. 5(b). The direct bandgap value of the compound Ba<sub>2</sub>Gd<sub>2/3</sub>□<sub>1/3</sub>Mn<sub>2</sub>Te<sub>5</sub> was found to be 1.06(2) eV. The indirect bandgap was also estimated, and it was found to be 0.81(2) eV. Thus, it is safe to conclude that Ba<sub>2</sub>Gd<sub>2/3</sub>□<sub>1/3</sub>Mn<sub>2</sub>Te<sub>5</sub> is a narrow bandgap semiconductor.

### 3.4. Temperature-dependent resistivity study of Ba<sub>2</sub>Gd<sub>2/3</sub>□<sub>1/3</sub>Mn<sub>2</sub>Te<sub>5</sub>

Fig. 6 shows the variation in the dc-electrical resistivity of a polycrystalline Ba<sub>2</sub>Gd<sub>2/3</sub>□<sub>1/3</sub>Mn<sub>2</sub>Te<sub>5</sub> sample with temperature. The resistivity starts to increase exponentially upon cooling the sample below room temperature. This behavior is character-

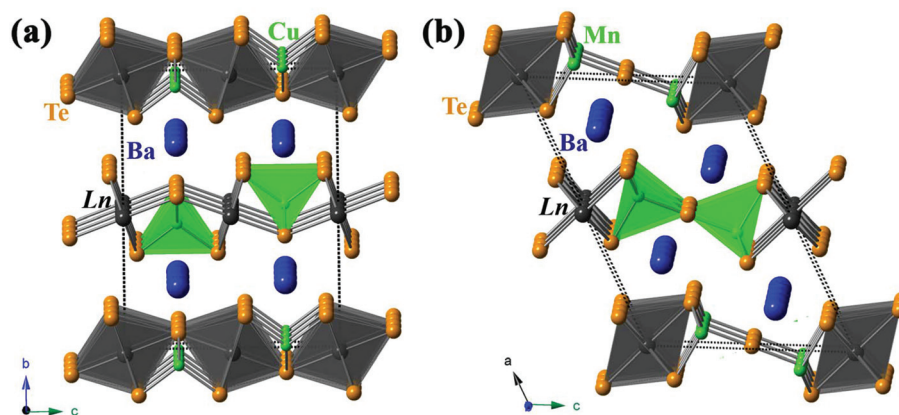


Fig. 4 The unit cell views of (a) BaLnCuTe<sub>3</sub><sup>10</sup> and (b) Ba<sub>2</sub>Ln<sub>1-x</sub>Mn<sub>2</sub>Te<sub>5</sub> structures.

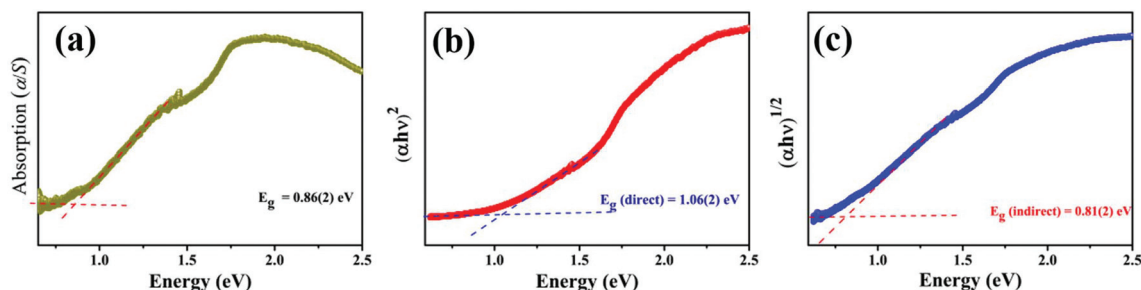


Fig. 5 (a) The optical absorption spectrum, (b) the direct, and (c) indirect bandgap Tauc plots for polycrystalline  $\text{Ba}_2\text{Gd}_{2/3}\square_{1/3}\text{Mn}_2\text{Te}_5$ .

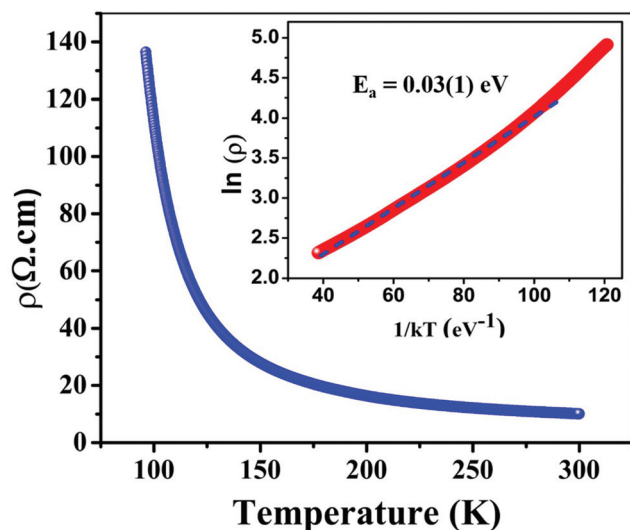


Fig. 6 The temperature-dependent resistivity plot for polycrystalline  $\text{Ba}_2\text{Gd}_{2/3}\square_{1/3}\text{Mn}_2\text{Te}_5$ . The inset shows the corresponding Arrhenius plot for  $\text{Ba}_2\text{Gd}_{2/3}\square_{1/3}\text{Mn}_2\text{Te}_5$ .

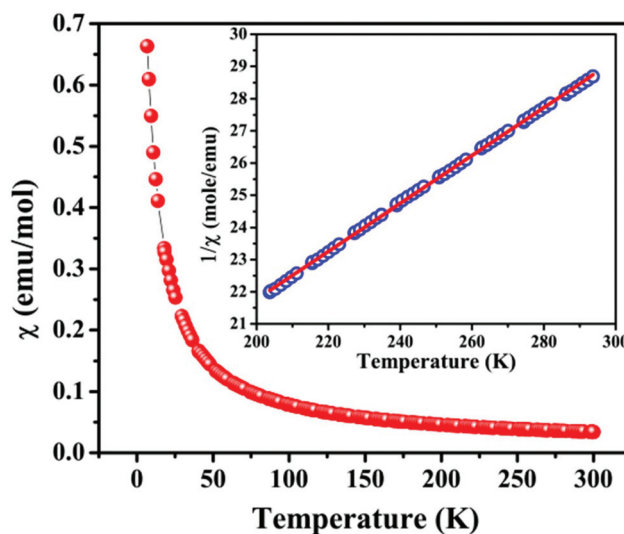


Fig. 7 Temperature dependence of the molar magnetic susceptibility ( $\chi_{\text{mol}}$ ) of  $\text{Ba}_2\text{Gd}_{2/3}\square_{1/3}\text{Mn}_2\text{Te}_5$  powder under an applied magnetic field of 1000 Oe. The inset of the figure shows a linear Curie–Weiss fitting of the inverse magnetic susceptibility data in the temperature range of 200–300 K.

istic of a semiconducting sample. The room temperature value of resistivity was found to be about 10  $\Omega$  cm. The semiconducting nature of the  $\text{Ba}_2\text{Gd}_{2/3}\square_{1/3}\text{Mn}_2\text{Te}_5$  sample is also consistent with the optical absorption bandgap study.

To estimate the activation energy, we have plotted a graph (inset of Fig. 6) of  $\ln(\rho)$  vs.  $1/kT$  (in  $\text{eV}^{-1}$ ), which is known as the Arrhenius plot. The symbols  $\rho$  and  $k$  represent electrical resistivity and the Boltzmann constant, respectively. The Arrhenius plot showed a nearly straight line over a temperature region of 105–300 K. The activation energy was estimated to be about 0.03(2) eV from the slope of this line.

### 3.5. Magnetic properties of $\text{Ba}_2\text{Gd}_{2/3}\square_{1/3}\text{Mn}_2\text{Te}_5$

The temperature-dependent magnetization studies of a polycrystalline sample of  $\text{Ba}_2\text{Gd}_{2/3}\square_{1/3}\text{Mn}_2\text{Te}_5$  were carried out over the temperature region of 5 K–300 K. The temperature-dependent magnetic susceptibility plot for  $\text{Ba}_2\text{Gd}_{2/3}\square_{1/3}\text{Mn}_2\text{Te}_5$  is shown in Fig. 7. The magnetic susceptibility ( $\chi$ ) was found to increase on cooling the sample till 5 K, with no evidence of long-range magnetic ordering. The inverse of magnetic susceptibility was plotted with temperature, and the data were fitted

linearly based on the modified Curie–Weiss law equation:  $\chi(T) = C/(T - \theta)$  to calculate values for the Curie constant ( $C$ ) and the Weiss constant ( $\theta$ ). The linear fit of inverse magnetic susceptibility against temperature (inset of Fig. 7) adheres to the Curie–Weiss law at the high-temperature range (200 K to 300 K). The calculated value of  $C$  was found to be 13.43(2)  $\text{emu K mol}^{-1}$  and a negative Weiss constant ( $\theta$ ) of  $-92.38(2)$  K was observed. The large negative Weiss constant indicates a substantial degree of local antiferromagnetic coupling of 4f and 3d electrons of  $\text{Gd}^{3+}$  and  $\text{Mn}^{2+}$ .<sup>22</sup> The effective magnetic moment ( $\mu_{\text{eff}}$ ) of  $10.37\mu_{\text{B}}$  calculated from the Curie–Weiss law, is in good agreement with the theoretical value ( $\mu_{\text{cal}}$ ) of  $10.58\mu_{\text{B}}$ . The value of  $\mu_{\text{cal}}$  was calculated using the formula  $\mu_{\text{cal}} = \{2/3 \times (\mu_{\text{Gd}^{3+}})^2 + 2 \times (\mu_{\text{Mn}^{2+}})^2\}^{1/2}$ .<sup>22</sup> The effective magnetic moment of  $\text{Ba}_2\text{Gd}_{2/3}\square_{1/3}\text{Mn}_2\text{Te}_5$  is due to the spin only contribution from the  $\text{Gd}^{3+}$  ( ${}^8\text{S}_{7/2}$ ) and  $\text{Mn}^{2+}$  ( ${}^6\text{S}_{5/2}$ ) ions as their orbital magnetic moment value is zero.

A nonlinear fitting of the inverse of magnetic susceptibility data with temperature was also performed based on the

equation  $\chi(T) = \chi_D + C/(T - \theta)$  to estimate the effect of diamagnetic susceptibility contributions ( $\chi_D$ ) to the  $C$  and  $\theta$  values. The diamagnetic susceptibility ( $\chi_D$ ) value obtained from the above non-linear equation is  $-3.24 \times 10^{-4} \text{ emu mol}^{-1}$ , which is very small and comparable with the theoretical value of  $-2.77 \times 10^{-4} \text{ emu mol}^{-1}$ ,<sup>63</sup> and hence can be neglected since it does not affect the values of  $C$  and  $\theta$  values obtained from the linear fit.

### 3.6. Electronic structure of $\text{Ba}_2\text{Gd}_{2/3}\square_{1/3}\text{Mn}_2\text{Te}_5$

The spin-polarized and non-polarized calculations were performed using the GGA+U method to explore the atomic and electronic structure of  $\text{Ba}_2\text{Gd}_{2/3}\square_{1/3}\text{Mn}_2\text{Te}_5$ , which could also be considered as  $\text{Ba}_6\text{Gd}_2\square\text{Mn}_6\text{Te}_{15}$  as discussed in section 2.7.

Table 5 shows the fractional coordinates of atoms in the unit cell obtained from the spin-polarized calculation with  $U = 2 \text{ eV}$  for Mn-3d orbitals. As can be seen, the theoretical estimates are in good agreement (<3%) with the experiments. For spin-polarized calculations, the antiferromagnetic configuration is found to be lower in energy by  $\sim 200 \text{ meV f.u}^{-1}$  as compared to the ferromagnetic configuration and thereby more stable. The absolute value of the magnetic moment of each Mn atom is found to be  $\sim 4.3\mu_B$ . In our calculations, only antiferromagnetic (AF) ordering, where the (010) intra-plane coupling is ferromagnetic while the (010) inter-plane coupling is antiferromagnetic, is considered. This AF ordering is similar to the A-type ordering generally considered in the perovskite magnetic oxides. However, it may be noted that though AF ordering is found to be more stable, the true ground state may consist of a more complex spin structure or magnetic ordering. Furthermore, nanoregions with a different type of AF ordering and/or competing magnetic spin structures may also exist in the system.<sup>64,65</sup>

Fig. 8 shows the total density of states (DOS) for the antiferromagnetic, ferromagnetic, and non-magnetic configur-

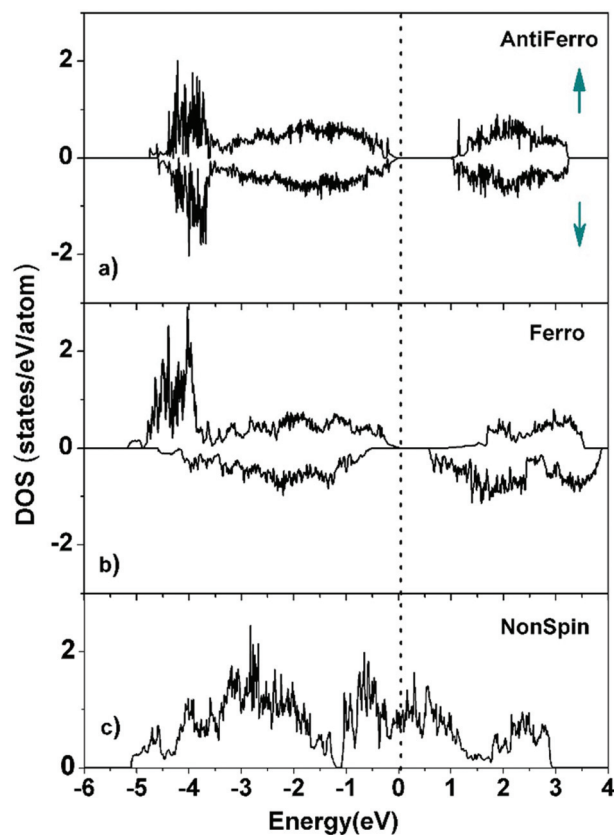


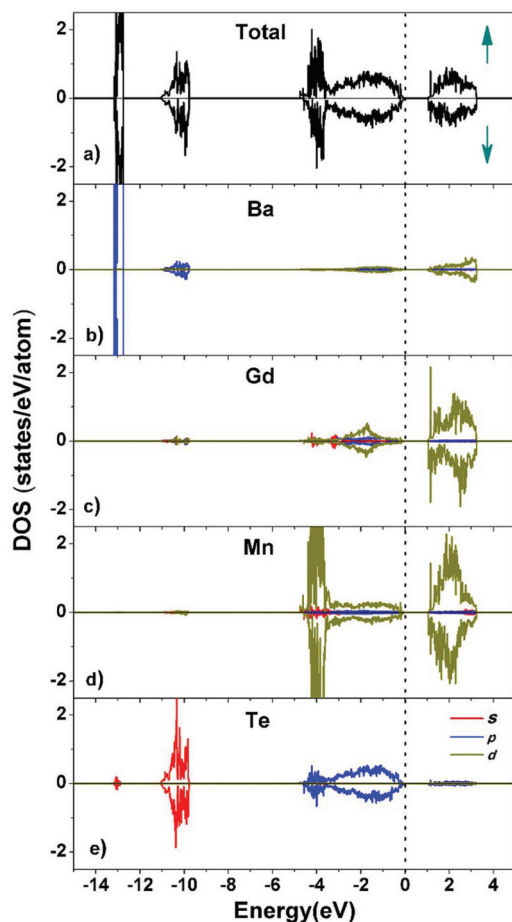
Fig. 8 The total density of states for  $\text{Ba}_2\text{Gd}_{2/3}\square_{1/3}\text{Mn}_2\text{Te}_5$  in the (a) anti-ferromagnetic, (b) ferro, and (c) non-spin configurations. The densities of the spin-up and spin-down states are indicated by the positive (up arrow) and negative values (down arrow).

Table 5 The computed fractional atomic coordinates of a  $\text{Ba}_2\text{Gd}_{2/3}\square_{1/3}\text{Mn}_2\text{Te}_5$  unit cell

Site		$x$	$y$	$z$
Ba-1	Cal. (exp.)	0.175 (0.1744)	0.000 (0.0)	0.716 (0.7281)
Ba-2	Cal. (exp.)	0.675 (0.6744)	0.500 (0.5)	0.716 (0.7281)
Ba-3	Cal. (exp.)	0.825 (0.8256)	0.000 (0.0)	0.284 (0.2719)
Ba-4	Cal. (exp.)	0.325 (0.3256)	0.500 (0.5)	0.284 (0.2719)
Gd-1	Cal. (exp.)	0.0 (0.0)	-0.026 (0.0)	0.0 (0.0)
Gd-2	Cal. (exp.)	0.500 (0.5)	0.526 (0.5)	0.001 (0.0)
Mn-1	Cal. (exp.)	0.562 (0.563)	0.000 (0.0)	0.290 (0.3016)
Mn-2	Cal. (exp.)	0.061 (0.063)	0.499 (0.5)	0.289 (0.3016)
Mn-3	Cal. (exp.)	0.438 (0.437)	0.001 (0.0)	0.710 (0.6983)
Mn-4	Cal. (exp.)	0.938 (0.937)	0.499 (0.5)	0.709 (0.6983)
Te-1	Cal. (exp.)	0.181 (0.1641)	0.001 (0.0)	0.357 (0.312)
Te-2	Cal. (exp.)	0.656 (0.6641)	0.518 (0.5)	0.318 (0.312)
Te-3	Cal. (exp.)	0.819 (0.8359)	0.000 (0.0)	0.642 (0.688)
Te-4	Cal. (exp.)	0.344 (0.3359)	0.516 (0.5)	0.682 (0.688)
Te-5	Cal. (exp.)	0.384 (0.3855)	0.000 (0.0)	0.059 (0.0639)
Te-6	Cal. (exp.)	0.878 (0.8855)	0.504 (0.5)	0.058 (0.0639)
Te-7	Cal. (exp.)	0.616 (0.6144)	0.000 (0.0)	0.941 (0.9361)
Te-8	Cal. (exp.)	0.122 (0.1144)	0.504 (0.5)	0.941 (0.9361)
Te-9	Cal. (exp.)	0.0 (0.0)	0.498 (0.5)	0.5 (0.5)
Te-10	Cal. (exp.)	0.5 (0.5)	0.0 (0.0)	0.5 (0.5)

ations. As can be seen, the bandgap is found to be  $\sim 0.97 \text{ eV}$  for the antiferromagnetic and  $\sim 0.54 \text{ eV}$  for the ferromagnetic configurations. However, the bandgap disappears for the non-magnetic configuration. This suggests that the appearance of the bandgap in  $\text{Ba}_2\text{Gd}_{2/3}\square_{1/3}\text{Mn}_2\text{Te}_5$  is strongly related to the underlying magnetic structure and thereby exchange interactions. It may be noted that different values of the  $U$  (on-site Coulomb correlations) parameter for Mn-3d orbitals, usually in the range 2.0–5.0 eV, have been used in several earlier reported works.<sup>66,67</sup> Thus, in order to test the dependence of the bandgap magnitude on the  $U$  parameter, we have also performed electronic structure calculations with different values of  $U$ , i.e.,  $U = 2 \text{ eV}$ ,  $3 \text{ eV}$ , and  $3.9 \text{ eV}$ . The bandgap is found to be increased by  $\sim 0.14 \text{ eV}$  as  $U$  is increased from 2 eV to 5 eV. The bandgap is computed to be 1.06 eV and 1.09 eV for  $U = 3.0 \text{ eV}$  and  $U = 4.0 \text{ eV}$ , respectively, for the AF configuration.

Next, the spin-polarized total and projected densities of the electronic states of  $\text{Ba}_2\text{Gd}_{2/3}\square_{1/3}\text{Mn}_2\text{Te}_5$  (AF configuration) shown in Fig. 9 are analyzed. The valence band (VB) width is  $\sim 5 \text{ eV}$  with VB extending from  $\sim -5.5 \text{ eV}$  to valence band maximum (VBM) at 0 eV. The states in the VB from 0 to  $-3 \text{ eV}$  are mainly comprised of Te-5p along with a lesser contribution from the Mn-3d orbitals. The VB in the energy range of  $-3 \text{ eV}$



**Fig. 9** (a) The total density of states for  $\text{Ba}_2\text{Gd}_{2/3}\square_{1/3}\text{Mn}_2\text{Te}_5$  with anti-ferromagnetic ordering for Mn magnetic moments. (b) The partial density of states (PDOS) projected onto the orbitals of Ba atom, (c) Gd atom, (d) Mn atom, and (e) Te atom.

to  $-5$  eV is predominantly comprised of the Mn-3d orbitals. The states from  $-9.5$  eV to  $-11$  eV are primarily contributed by the Te-4s orbitals. The states at  $\sim -13$  eV are primarily the Ba-5p states. The conduction band ( $\sim 1$  eV to 3 eV) is comprised of the Mn-3d and Gd-5d orbitals.

## 4. Conclusions

Three new quaternary compounds of  $\text{Ba}_2\text{Ln}_{1-x}\text{Mn}_2\text{Te}_5$  (Ln = Pr, Gd, and Yb) were successfully synthesized by the exploratory solid-state sealed tube method. The single-crystal X-ray diffraction studies show that these compounds crystallize in the monoclinic  $C2/m$  space group. In these structures, all atomic sites are fully occupied except the Ln1 site, which shows an occupational disorder: only two-thirds of the Ln sites are filled for the Pr and Gd compounds. The crystal structures of these compounds can be viewed as a defect variant of the  $\text{Ba}_2\text{UCu}_2\text{S}_5$  structure type. There are six crystallographically unique sites in a unit cell: one Ba (site symmetry:  $.m.$ ), one Mn ( $.m.$ ), one Ln, and three Te atoms. The building blocks of these structures are based on Ln-

based octahedra ( $\text{LnTe}_6$ ) and Mn-based tetrahedra ( $\text{MnTe}_4$ ). These  $\text{LnTe}_6$  and  $\text{MnTe}_4$  units are condensed to form the  ${}^2_{\infty}[\text{Ln}_{1-x}\text{Mn}_2\text{Te}_5]^{4-}$  layers that are separated by the  $\text{Ba}^{2+}$  cations. The optical absorption study of the polycrystalline  $\text{Ba}_2\text{Gd}_{2/3}\square_{1/3}\text{Mn}_2\text{Te}_5$  compound shows the direct and indirect bandgaps of 1.06(2) eV and 0.81(2) eV, respectively, which are in good agreement with the theoretical study and consistent with the black color of the compound. The temperature-dependent resistivity study confirms the semiconducting behavior of polycrystalline  $\text{Ba}_2\text{Gd}_{2/3}\square_{1/3}\text{Mn}_2\text{Te}_5$ . The magnetic studies of polycrystalline  $\text{Ba}_2\text{Gd}_{2/3}\square_{1/3}\text{Mn}_2\text{Te}_5$  did not show any long-range ordering down to 5 K. The narrow bandgap of  $\text{Ba}_2\text{Gd}_{2/3}\square_{1/3}\text{Mn}_2\text{Te}_5$  is promising for future thermoelectric studies.

## Conflicts of interest

There are no conflicts to declare.

## Acknowledgements

JP thanks DST-SERB, Government of India for the financial support under the early career research (ECR) award (grant number: ECR/2017/000822) and IIT Hyderabad for seed grant and research facilities. SJ and GP thank MHRD, IIT Hyderabad for the research fellowships. MI thanks DST India for the research fellowship. The authors also gratefully acknowledge DST-FIST (SR/FST/ETI-421/2016) for the SEM-EDS facility and DST-FIST (SR/FST/PSI-215/2016) for computational resources used in this work. The authors thank Prof. James A. Ibers (Northwestern University, USA) for helpful discussions on crystal structure refinements.

## References

- 1 C.-Y. Meng, H. Chen, P. Wang and L. Chen, *Chem. Mater.*, 2011, **23**, 4910–4919.
- 2 A. Assoud, S. Thomas, B. Sutherland, H. Zhang, T. M. Tritt and H. Kleinke, *Chem. Mater.*, 2006, **18**, 3866–3872.
- 3 Z. Guo, F. Sun and W. Yuan, *Cryst. Growth Des.*, 2017, **17**, 2238–2253.
- 4 A. P. Tiwari, T. G. Novak, X. Bu, J. C. Ho and S. Jeon, *Catalysts*, 2018, **8**, 551.
- 5 M. Sturza, J. M. Allred, C. D. Malliakas, D. E. Bugaris, F. Han, D. Y. Chung and M. G. Kanatzidis, *Chem. Mater.*, 2015, **27**, 3280–3290.
- 6 O. Massenet, J. J. Since, J. Mercier, M. Avignon, R. Buder, V. D. Nguyen and J. Kelber, *J. Phys. Chem. Solids*, 1979, **40**, 573–577.
- 7 O. Peña and M. Sergent, *Prog. Solid State Chem.*, 1989, **19**, 165–281.
- 8 K. Mitchell and J. A. Ibers, *Chem. Rev.*, 2002, **102**, 1929–1952.
- 9 I. Ijjaali, A. D. McFarland, C. L. Haynes, R. P. Van Duyne and J. A. Ibers, *J. Solid State Chem.*, 2003, **172**, 127–131.

- 10 Y. Yang and J. A. Ibers, *J. Solid State Chem.*, 1999, **147**, 366–371.
- 11 F. Q. Huang and J. A. Ibers, *Inorg. Chem.*, 1999, **38**, 5978–5983.
- 12 R. Patschke, P. Brazis, C. R. Kannewurf and M. Kanatzidis, *Inorg. Chem.*, 1998, **37**, 6562–6563.
- 13 W. Yin, A. K. Iyer, X. Lin, C. Li, J. Yao and A. Mar, *Dalton Trans.*, 2016, **45**, 12329–12337.
- 14 H. K. Vivanco and E. E. Rodriguez, *J. Solid State Chem.*, 2016, **242**, 3–21.
- 15 J. Guo, S. Jin, G. Wang, S. Wang, K. Zhu, T. Zhou, M. He and X. Chen, *Phys. Rev. B: Condens. Matter Mater. Phys.*, 2010, **82**, 180520.
- 16 T. P. Ying, X. L. Chen, G. Wang, S. F. Jin, T. T. Zhou, X. F. Lai, H. Zhang and W. Y. Wang, *Sci. Rep.*, 2012, **2**, 426.
- 17 K. H. J. Buschow, *Rep. Prog. Phys.*, 1977, **40**, 1179–1256.
- 18 M. Wakeshima and Y. Hinatsu, *J. Solid State Chem.*, 2001, **159**, 163–169.
- 19 M. Wakeshima and Y. Hinatsu, *J. Solid State Chem.*, 2000, **153**, 330–335.
- 20 P. Wu, A. E. Christuk and J. A. Ibers, *J. Solid State Chem.*, 1994, **110**, 337–344.
- 21 Y. Liu, L. Chen, L.-M. Wu, G. H. Chan and R. P. Van Duyne, *Inorg. Chem.*, 2008, **47**, 855–862.
- 22 K. Mitchell, F. Q. Huang, E. N. Caspi, A. D. McFarland, C. L. Haynes, R. C. Somers, J. D. Jorgensen, R. P. Van Duyne and J. A. Ibers, *Inorg. Chem.*, 2004, **43**, 1082–1089.
- 23 K. Pal, Y. Xia, J. He and C. Wolverton, *Phys. Rev. Mater.*, 2019, **3**, 085402.
- 24 The inorganic crystal structure database (ICSD) web, <https://icsd.fiz-karlsruhe.de/index.xhtml>, Accessed date: 16 February 2021.
- 25 L. A. Koscielski and J. A. Ibers, *Z. Anorg. Allg. Chem.*, 2012, **638**, 2585–2593.
- 26 Agilent, *P.R.O. CrysAlis*, Agilent Technologies Ltd, Yarnton, Oxfordshire, England, 2014.
- 27 SCALE3 ABSPACK - an Oxford Diffraction Program (1.0.4, gui:1.0.3) (C), Oxford Diffraction Ltd., 2005 (n.d.).
- 28 APEX3: Program for Data Collection on Area Detectors, Bruker AXS Inc., Madison, WI, USA, 2016.
- 29 G. M. Sheldrick, *SADABS*, Department of Structural Chemistry, University of Göttingen, Göttingen, Germany, 2008.
- 30 G. M. Sheldrick, *Acta Crystallogr., Sect. C: Struct. Chem.*, 2015, **71**, 3–8.
- 31 G. M. Sheldrick, *XPREP Version 2008/2*, Bruker AXS Inc., Madison, 2008.
- 32 G. M. Sheldrick, *Acta Crystallogr., Sect. A: Found. Crystallogr.*, 2008, **64**, 112–122.
- 33 A. L. Spek, *PLATON, A Multipurpose Crystallographic Tool*, Utrecht University, Utrecht, The Netherlands, 2014.
- 34 L. M. Gelato and E. Parthé, *J. Appl. Crystallogr.*, 1987, **20**, 139–143.
- 35 Match! - Phase Analysis using Powder Diffraction <https://www.crystalimpact.de/match/>, (accessed February 16, 2021).
- 36 G. Kortüm, *Reflectance Spectroscopy: Principles, Methods, Applications*, Springer-Verlag, Berlin Heidelberg, 1969.
- 37 S. Jana, M. Ishtiyak, A. Mesbah, S. Lebègue, J. Prakash, C. D. Malliakas and J. A. Ibers, *Inorg. Chem.*, 2019, **58**, 7837–7844.
- 38 W. Kohn and L. J. Sham, *Phys. Rev.*, 1965, **140**, A1133–A1138.
- 39 G. Kresse and J. Furthmüller, *Phys. Rev. B: Condens. Matter Mater. Phys.*, 1996, **54**, 11169–11186.
- 40 P. E. Blöchl, *Phys. Rev. B: Condens. Matter Mater. Phys.*, 1994, **50**, 17953–17979.
- 41 S. L. Dudarev, G. A. Botton, S. Y. Savrasov, C. J. Humphreys and A. P. Sutton, *Phys. Rev. B: Condens. Matter Mater. Phys.*, 1998, **57**, 1505–1509.
- 42 J. P. Perdew, K. Burke and M. Ernzerhof, *Phys. Rev. Lett.*, 1996, **77**, 3865–3868.
- 43 M. A. Greaney, K. V. Ramanujachary, Z. Teweldemedhin and M. Greenblatt, *J. Solid State Chem.*, 1993, **107**, 554–562.
- 44 H. Zeng, J. Yao and J. A. Ibers, *J. Solid State Chem.*, 2008, **181**, 552–555.
- 45 J. Yao, B. Deng, L. J. Sherry, A. D. McFarland, D. E. Ellis, R. P. Van Duyne and J. A. Ibers, *Inorg. Chem.*, 2004, **43**, 7735–7740.
- 46 R. Baumbach, L. Balicas, G. T. McCandless, P. Sotelo, Q. R. Zhang, J. Evans, D. Camdzic, T. J. Martin, J. Y. Chan and R. T. Macaluso, *J. Solid State Chem.*, 2019, **269**, 553–557.
- 47 C.-Y. Meng, H. Chen and P. Wang, *Inorg. Chem.*, 2014, **53**, 6893–6903.
- 48 R. D. Shannon, *Acta Crystallogr., Sect. A: Cryst. Phys., Diffr., Theor. Gen. Crystallogr.*, 1976, **32**, 751–767.
- 49 J. F. Miller, L. K. Matson and R. C. Himes, *Proceedings of the Conference on Rare Earths Research*, 1961, 2nd (1962) edn, pp. 233–248.
- 50 A. Bentien, S. Budnyk, Yu. Prots, Yu. Grin and F. Steglich, *J. Alloys Compd.*, 2007, **442**, 345–347.
- 51 H. Lin, J.-N. Shen, L. Chen and L.-M. Wu, *Inorg. Chem.*, 2013, **52**, 10726–10728.
- 52 E. J. Wu and J. A. Ibers, *Acta Crystallogr., Sect. C: Cryst. Struct. Commun.*, 1997, **53**, 993–994.
- 53 W. Yin, W. Wang, L. Bai, K. Feng, Y. Shi, W. Hao, J. Yao and Y. Wu, *Inorg. Chem.*, 2012, **51**, 11736–11744.
- 54 J. Prakash, A. Mesbah, J. Beard, D. Rocca, S. Lebègue, C. D. Malliakas and J. A. Ibers, *Z. Naturforsch., B: J. Chem. Sci.*, 2016, **71**, 425–429.
- 55 S. Maier, J. Prakash, D. Berthebaud, O. Perez, S. Bobev and F. Gascoin, *J. Solid State Chem.*, 2016, **242**, 14–20.
- 56 F. Q. Huang, K. Mitchell and J. A. Ibers, *Inorg. Chem.*, 2001, **40**, 5123–5126.
- 57 N. E. Brese and M. O'Keeffe, *Acta Crystallogr., Sect. B: Struct. Sci.*, 1991, **47**, 192–197.
- 58 A. Altomare, C. Cuocci, C. Giacovazzo, A. Moliterni, R. Rizzi, N. Corriero and A. Falcicchio, *J. Appl. Crystallogr.*, 2013, **46**, 1231–1235.
- 59 F. Liebau and X. Wang, *Acta Crystallogr., Sect. B: Struct. Sci.*, 2008, **64**, 299–304.

- 60 G. A. Williams, B. N. Figgis and F. H. Moore, *Acta Crystallogr., Sect. B: Struct. Crystallogr. Cryst. Chem.*, 1980, **36**, 2893–2897.
- 61 P. Lemoine, D. Carré and M. Guittard, *Acta Crystallogr., Sect. C: Cryst. Struct. Commun.*, 1986, **42**, 390–391.
- 62 M. F. Mansuetto, P. M. Keane and J. A. Ibers, *J. Solid State Chem.*, 1992, **101**, 257–264.
- 63 G. A. Bain and J. F. Berry, *J. Chem. Educ.*, 2008, **85**, 532–536.
- 64 J. M. D. Coey, *Magnetism and Magnetic Materials*, Cambridge University Press, Cambridge, 2010.
- 65 M. K. Niranjana, B. R. Sahu and L. Kleinman, *Phys. Rev. B: Condens. Matter Mater. Phys.*, 2004, **70**, 180406.
- 66 K. Leung, S. B. Rempe, P. A. Schultz, E. M. Sproviero, V. S. Batista, M. E. Chandross and C. J. Medforth, *J. Am. Chem. Soc.*, 2006, **128**, 3659–3668.
- 67 J. Li, *Sci. Rep.*, 2016, **6**, 22422.